



1 **Thermal dissociation cavity enhanced absorption spectrometer for detecting NO₂,**
2 **RO₂NO₂ and RONO₂ in the atmosphere**

3 Chunmeng Li¹, Haichao Wang^{1, 2, 3*}, Xiaorui Chen¹, Tianyu Zhai¹, Shiyi Chen¹, Xin Li¹, Limin Zeng¹, Keding Lu^{1, *}

4 ¹ State Key Joint Laboratory of Environmental Simulation and Pollution Control, College of Environmental Sciences
5 and Engineering, Peking University, Beijing, 100871, China.

6 ² School of Atmospheric Sciences, Sun Yat-sen University, Zhuhai, Guangdong, 510275, China.

7 ³ Guangdong Provincial Observation and Research Station for Climate Environment and Air Quality Change in the
8 Pearl River Estuary, Key Laboratory of Tropical Atmosphere-Ocean System, Ministry of Education, Southern
9 Marine Science and Engineering Guangdong Laboratory (Zhuhai), Zhuhai, 519082, China.

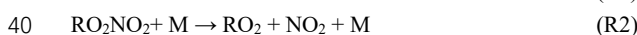
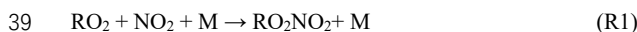
10 * Corresponding author: wanghch27@mail.sysu.edu.cn; k.lu@pku.edu.cn

11 **Abstract.** We developed a thermal dissociation cavity enhanced absorption spectroscopy (TD-CEAS) for the in-situ
12 measurement of NO₂, total peroxy nitrates (PNs, RO₂NO₂), and total alkyl nitrates (ANs, RONO₂) in the atmosphere. PNs
13 and ANs are thermally converted to NO₂ at the corresponding pyrolysis temperatures and detected by CEAS at 435 - 455
14 nm. The instrument samples sequentially from three channels at ambient temperature, 453K and 653K, with a cycle of 3
15 minutes, for measuring NO₂, NO₂+PNs, and NO₂+PNs+ANs, respectively. The absorptions between the three channels are
16 used to derive the mixing ratios of PNs and ANs by the spectral fitting. The limit of detection (LOD) is estimated to be 97
17 pptv (1σ) at 6 s intervals for NO₂. The measurement uncertainty of NO₂ is estimated to be 8%, while the uncertainties of
18 PNs and ANs detection is larger than NO₂ due to some chemical interferences in the heating channels, such as the reaction
19 of NO (or NO₂) with the peroxy radicals produced by the thermal dissociation of organic nitrates. Based on the laboratory
20 experiments and numerical simulations, we set up a lookup table method to correct these interferences in PNs and ANs
21 channel under various concentrations of ambient organic nitrates, NO, and NO₂. Finally, we present the first field
22 deployment and compared it with other instruments during a field campaign in China, the advantage and limitations of this
23 instrument are outlined.

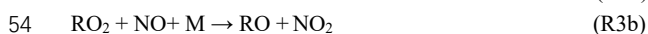
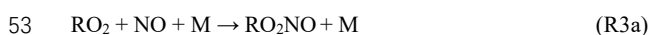


24 1. Introduction

25 Organic nitrates (ONs) act as the temporary NO_x reservoir species, which affects the atmospheric circulation and has
26 impacts on air quality and climate (Mellouki et al., 2015). Peroxy nitrates (PNs, RO₂NO₂) and alkyl nitrates (ANs,
27 RONO₂) are the two important kinds of organic nitrates. They are closely related to the distribution of oxidants in the
28 atmosphere by terminating HO_x cycle. ONs are also the important precursors of secondary organic aerosol (SOA)
29 (Berkemeier et al., 2016; Lee et al., 2016; Ng et al., 2017; Rollins et al., 2012). Volatile organic compounds (VOCs)
30 are oxidized by OH or O₃ to produce peroxy radicals (RO₂), then the RO₂ reacts with NO₂ to produce PNs (R1). In
31 addition, the aldehydes formed during the process of NO₃ oxidizing isoprene at night react with NO₃ to form PNs.
32 PNs can be divided into two categories depending on the nature of the RO₂ group. One is peroxy acyl nitrates (PANs)
33 when RO₂ is R'C(O)OO, among which PPN (peroxypropionyl nitrate) and PAN dominate PNs with the percentage
34 of 75%-90% due to the relatively high thermal stability. While some peroxy nitrates without acyl group are only
35 abundant in the cold regions (Roberts, 1990; Roberts et al., 1998b; Thieser et al., 2016; Wooldridge et al., 2010). The
36 sink pathways of PNs include deposition, thermal decomposition, photolysis, and OH oxidation, and the thermal
37 decomposition dominates in the troposphere with a temperature dependence (R2). Therefore, the lifetime of PAN is
38 various from less than one hour to several months, depending on the environmental conditions.



41 At the high NO_x region, RO₂ reacts primarily with NO to produce ANs. ANs can be also emitted directly from
42 biomass combustion and the ocean. The ocean emission is regarded as the main source of short-chain ANs (C₁-C₃),
43 and up to tens of pptv of species above have been measured in marine areas (Atlas et al., 1993; Chuck et al., 2002;
44 Talbot et al., 2000). The NO₃-initiated ANs during the night is generally considered to be important, which has a
45 higher organic nitrate yield compared with OH-initiated ANs (Horowitz et al., 2007; Perring et al., 2013). During the
46 daytime, there is a branch reaction in forming ANs (R3) with a small branch ratio (1%-30%) (Arey et al., 2001;
47 Reisen et al., 2005; Russell and Allen, 2005; Wennberg et al., 2018). Ambient ANs are removed by photolysis or
48 oxidation to produce NO_x or HNO₃, be deposited or transported as NO_x reservoirs. ANs play a significant role in
49 SOA formation (Lee et al., 2016; Zare et al., 2018). Monofunctional ANs are stable and account for a small proportion
50 of ANs, among which the ones formed from alkanes can be the tracers of human activities in remote areas (Simpson
51 et al., 2006; Wang et al., 2003). Polyfunctional ANs are hard to detect since they are more reactive than
52 monofunctional ANs.



55 The various sources and sinks of ONs complicate their atmospheric distribution. The measurement of ANs and
56 PNs has been developed by gas chromatography (GC). GC is used for separation of species, and then the separated
57 substances are quantified by using electron capture detectors (ECD), luminol chemiluminescence (CL), or mass
58 spectrometry (MS) (Atlas, 1988; Blanchard et al., 1993; Flocke et al., 2005; Gaffney et al., 1998; Hao et al., 1994;
59 Luxenhofer et al., 1994; Tanimoto et al., 1999). These methods measure individual species accurately (Roberts et al.,
60 2003), but the individual standards are incomprehensive. Meanwhile, the methods suffer from relatively low time
61 resolution (Blanchard et al., 1993). Day et al. (2002) used the feature of gradient pyrolysis of reactive nitrogen
62 compounds and determined NO₂ product by TD-LIF (thermal-dissociation laser-induced fluorescence), achieving the
63 measurement of PNs, ANs, and gaseous HNO₃ (Day et al., 2002). After that, chemical ionization mass spectrometry
64 (CIMS) and cavity enhanced spectroscopy have been used to quantify the pyrolysis products (Paul and Osthoff, 2010;
65 Slusher et al., 2004; Thieser et al., 2016; Wild et al., 2014). The detection limits and response times of TD-CIMS are
66 excellent, but ¹³C-labeled PAN is required as an internal standard. TD-CRDS (cavity ring-down spectroscopy) and



67 TD-CAPS (cavity attenuated phase shift spectroscopy) have achieved measurements of PNs and ANs (Sadanaga et
68 al., 2016; Sobanski et al., 2016), which showed high spatial and temporal resolution and good measurement capability.
69 Organic nitrates have a large range of mixing ratios in the atmosphere that vary from several pptv in the warm and
70 remote regions to several ppbv in polluted regions. The field measurements of organic nitrates have been extensively
71 conducted in the United States and Europe (Fischer et al., 2000; Glavas and Moschonas, 2001; Kastler and
72 Ballschmiter, 1999; Perring et al., 2009; Roberts et al., 1998a; Sobanski et al., 2017), but the related studies are
73 sparse in China (Chen et al., 2017; Song et al., 2018; Sun et al., 2018; Zhang et al., 2018). Ozone pollution in China
74 has occurred frequently in recent years (Ma et al., 2019; Shu et al., 2019; Wang et al., 2009; Wang et al., 2017b; Yin
75 et al., 2019), but the importance of PNs and ANs in regulating ozone formation has not been well studied. Here we
76 developed a pyrolysis measurement system based on cavity enhanced absorption spectroscopy (CEAS) to detect NO₂,
77 PNs, and ANs in the atmosphere. In this study, the detailed setup of the instrument, laboratory characterizations, and
78 its first field applications in China are presented.

79 2. Methods

80 2.1 Instrumentation of TD-CEAS

81 Our instrument is designed to measure NO₂, ANs and PNs in the atmosphere, which has the characteristics of good
82 stability, low energy consumption and portability. The total weight of the instrument is less than 30 kg, the overall
83 size is 110 × 60 × 50 cm, and the power consumption is less than 300 W. The measurement of NO₂ is achieved by
84 CEAS. Due to the feature of gradient pyrolysis of ANs and PNs, the sample gas flowing out from three different
85 channels contains the total amount of NO₂ at different temperatures. The gradient of NO₂ concentration absorption
86 at different pyrolysis temperatures is used to retrieve the mixing ratio of NO₂, PNs, and ANs. The time resolution of
87 the instrument measurement is 6 s, the measurement time of each channel is 1 minute, and each cycle is 3 minutes.

88 The CEAS system has been described in detail in previous literature (Duan et al., 2018; Fiedler et al., 2003;
89 Gherman et al., 2008; Jordan and Osthoff, 2020; Jordan et al., 2019; Langridge et al., 2006; Liang et al., 2019; Liu
90 et al., 2019; Min et al., 2016; Tang et al., 2020; Ventrillard-Courtillot et al., 2010; Wang et al., 2017a; Yi et al., 2016),
91 so there is a brief introduction to the principle of the instrument. NO₂ molecules have a specific absorption structure
92 in the wavelength range of 400-500 nm (Fig. S1). Based on Lambert-Beer's law, the extinction coefficient (α) is
93 proportional to the absorber's concentration and the optical path. Here α is mainly contributed by the molecular
94 absorption, Rayleigh scattering and Mie scattering. Besides, it can also be obtained by comprehensive calculation
95 through the intensity of sampling spectrum, reference spectrum, mirror reflectivity, and effective cavity length (d_{eff}).

96 In Eq. 1, λ is the wavelength of light, $I_0(\lambda)$ is the intensity of the reference spectrum, $I(\lambda)$ is the sample spectrum,
97 d_{eff} is the effective cavity length (see Sec. 3.2 in detail), $R(\lambda)$ is the mirror reflectivity, $\alpha_{Mie}(\lambda)$ is the extinction
98 due to Mie scattering, $\alpha_{Rayl}(\lambda)$ is the extinction due to Rayleigh scattering, n_i and $\sigma_i(\lambda)$ are the number density
99 and absorption cross-section of i th gas compounds, respectively. According to Eq. 1, it is necessary to quantify the
100 mirror reflectivity, effective cavity length, and NO₂ absorption cross-section.

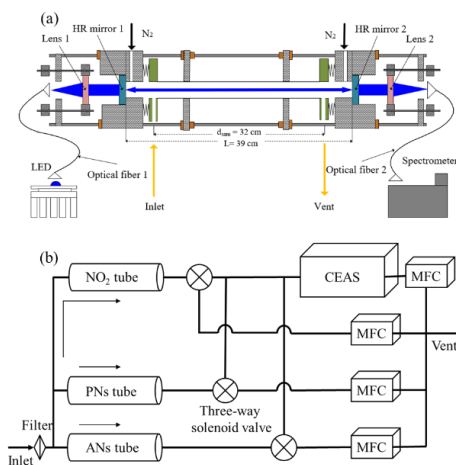
$$101 \alpha(\lambda) = \left(\frac{I_0(\lambda)}{I(\lambda)} - 1 \right) \left(\frac{1 - R(\lambda)}{d_{eff}} \right) \\ 102 = \sum_1 n_i \times \sigma_i(\lambda) + \alpha_{Mie}(\lambda) + \alpha_{Rayl}(\lambda) \quad (1)$$

103 As shown in Fig. 1a, the optical layout of the CEAS consists of the light source, collimating optics, cage system,
104 high-finesse cavity and a commercial spectrograph with a charge-coupled device (CCD) detector. The core of the
105 light source module is a single-color LED (M450D3, Thorlabs, Newton, NJ, USA), centering at 445 nm with a full
106 width at half maximum (FWHM) of 18 nm. To obtain a stable output of the light source, the input current and



107 operating temperature of the light source are stabilized to reduce the intensity and wavelength drift. The switching
108 power supply is 12 VDC with a current of 1.00 ± 0.01 A. The constant current control is achieved through a stable
109 current source. The temperature of the light source is controlled by the Proportion Integration Differentiation (PID)
110 algorithm and stabilized at 24.0 ± 0.1 °C.

111 Four stainless steel columns are used to collimate two opposing high-mirror mounting bases. The two endplates in
112 the middle of the cage structure further enhance the stability of the system. The light source is introduced into the
113 system through a fiber connected to a two-dimensional adjustment frame (CXY1, Thorlabs, Newton, NJ, USA)
114 through a connector. The plano-convex lens ($f = 30$ mm) is installed in another adjustment frame, and the two
115 adjustment frames are connected by a custom X-shaped adapter, which is fixed at the end with the light source. The
116 center alignment of the light source, the lens, and the high-reflectivity module are achieved by adjusting the
117 adjustment frame in the vertical and horizontal directions. Then blue light is thus introduced into an optical cavity
118 composed of a pair of high-reflectivity mirrors. The high-reflectivity mirror (CRD450-1025-100, Advanced thin films,
119 Colorado, USA) is reported to be greater than 0.9999 (440 – 460 nm) with a radius curvature of 1.0 m and a diameter
120 of 25.4 mm. The high-reflectivity mirrors are installed in the groove of the special custom base and sealed by an O-
121 ring, and then the three-dimensional micro-adjustment is achieved by squeezing the lens and the O-ring to adjust
122 their pitch and yaw finely. The distance between mirrors is 39.0 cm, and high-purity nitrogen ($> 99.999\%$), which
123 passes through the small hole before the mirror base, is used as a purge gas to protect the mirror surface.



124
125 Figure 1. The overall schematic of CEAS (a) and the instrument (b). CEAS is mainly composed of LED, collimating optics, cage structure,
126 high-finesse cavity and spectrometer. After filtering the PM, the gas goes through three quartz tubes, and then the alternate measurements
127 of NO_2 , NO_2+PNs and $\text{NO}_2+\text{PNs}+\text{ANs}$ is achieved by three-way solenoid valves.

128
129 The cavity system is sealed by two welded bellows, two polytetrafluoroethylenes (PTFE) connecting pieces, and
130 a stainless-steel sampling cell which is internally polished. The PTFE connecting piece connects the sampling cell
131 and the bellows and also acts as a sample inlet and outlet. As shown in Fig. 1a, the distance between the inlet and the
132 outlet (d_{sam}) is 32.0 cm. After passing through the sampling cavity, the blue light is converged by another plano-
133 convex mirror ($f = 50$ mm). It enters the detector-spectrometer (QE65PRO, Ocean Optics, Dunedin, FL, USA) for
134 signal acquisition through an optical fiber. The dark current in the CCD of the spectrometer is reduced by controlling
135 the temperature of CCD at -20.0 °C; the width of the entrance slit is 100 μm and the corresponding wavelength
136 resolution is 0.39 nm; the detection wavelength range is 413.48 - 485.48 nm.



137 The schematic of TD-CEAS is shown in Fig. 1b. The flow system mainly includes the particulate matter filtering
138 in the front end of the sampling line, the quartz tubes for species pyrolysis conversion, the three-way system switching
139 module, the detection module (CEAS) and the flow control module. The sample gas firstly passes through a PTFE
140 filter membrane (25 μm thickness, 4.6 cm diameter, 2.5 μm pore size, Typris, China) to remove ambient aerosols.
141 The sample gas enters the system through 1/4 inch PFA (polytetrafluoroethylene) tube, and then is divided into three
142 channels (NO_2 channel, ANs channel, and PNs channel) by using two T-shaped PFA three-way connection. The gas
143 flow at the end of each channel is controlled at 0.8 L min^{-1} and the total flow rate (sample flow gas and purge gas) is
144 2.6 L min^{-1} maintained by mass flow controllers and a diaphragm pump.

145 The quartz tubes have a length of 35 cm, which has an inner diameter of 5 mm and an outer diameter of 10 mm,
146 connected to the system through a 10 mm to 1/4 inch PTFE connection. The quartz tubes of the ANs channel and the
147 PNs channel are heated by resistance wire, and the temperature is controlled by the PID algorithm. An asbestos sleeve
148 on the quartz tube's surface is used to achieve the insulation of heat exchange with the external environment. The
149 heating power of PNs channel and ANs channel are about 20 W and 50 W, respectively. The length of the heating
150 module is 15 cm. According to the pyrolysis efficiency experiment (see Sec. 3.4 for details), the heating temperatures
151 for the ANs and PNs channels are controlled at $180 \text{ }^\circ\text{C}$ and $380 \text{ }^\circ\text{C}$, respectively. If it is assumed that the temperature
152 of the heating part is uniform, the gas residence times of the ANs and PNs channels are 92.3 ms and 141.9 ms,
153 respectively. One CEAS is used to detect the NO_2 absorption of different channels to reduce the cross-interference
154 due to the difference of multi-detectors. A solenoid valve is connected behind the quartz tube of each channel. At the
155 same time, a time relay is used to control the three T-shaped solenoid valves periodically. Each channel has the same
156 constant flow rate no matter the sampling air draw into the CEAS or vent. At the end of the channels, mass flow
157 controllers are used to restricting the flow rate.

158 2.2 Laboratory experiments setup

159 To characterize the performance and potential interferences of this instrument, we used a photochemical PAN source
160 in the laboratory experiments. Acetone undergoes photolysis at 285 nm from Hg lamp, and then generates excess PA
161 radicals (peroxyacetyl radicals) in the zero air. At this time, a small amount of NO reacts with PA to form NO_2 , and
162 then NO_2 further reacts with PA to form PAN. We got a standard PAN source in this way, which generated a source
163 at a level of 1-10 ppbv. The source level was double-checked by a GC-ECD instrument. To investigate the potential
164 interferences caused by the pyrolysis organic radical products react with ambient NO and NO_2 in TD-CEAS, a multi-
165 gas calibrator (146i, Thermo Fisher Scientific Inc., USA) was used to generate O_3 gas by photolysis of oxygen, and
166 output well-mixed gases by mixing NO or NO_2 with zero air according to the requirements. NO (1 ppmv) and NO_2
167 (10 ppmv) bottle gases were connected to the multi-gas calibrator. An ozone monitor was used to detecting O_3 levels
168 in these experiments (49i, Thermo Fisher Scientific Inc., USA). A NO_x monitor was used to detecting NO and NO_2
169 level in these experiments (42i, Thermo Fisher Scientific Inc., USA). Pure N_2 (>99.9999%) and He (>99.9999%)
170 bottle gas were used to calibrate the mirror reflectivity of CEAS and purge the mirrors.

171 2.3 Box model

172 A box model was established to mimic the experimental results and study the potential interferences of NO and NO_2
173 in PNs and ANs measurement. The chemical mechanism is followed by previous work (Thieser et al., 2016). These
174 reactions in the pyrolysis process in the box model are listed in Text S1, and the reaction rate of these reactions is
175 mainly taken from the MCM. As the wall loss has an important effect on the lifetime of free radicals, we set the wall
176 loss constant (k_{wall}) of RO_2 as the value of 0.3 /s (Thieser et al., 2016; Wooldridge et al., 2010). The wall loss rate
177 coefficients of HO_2 and OH are selected as the values of 0.5 and 5.4 /s (Fuchs et al., 2008). The residence time of the
178 sampling gas in each channel is calculated by considering the temperature distribution. The time step of the model is
179 set to 0.001s.



180 3. Instrument characterization

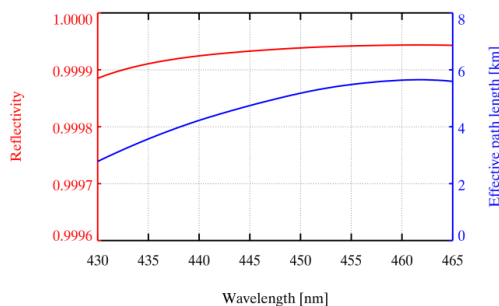
181 3.1 Mirror reflectivity

182 The spectra of the pure N₂ (>0.99999) or He (>0.99999) filling the cavity are collected to calibrate the mirror
 183 reflectivity, as the Rayleigh scattering section of the two is significantly distinct, so $R(\lambda)$ can be calibrated according
 184 to Eq.2 (Chen and Venables, 2011; Min et al., 2016).

$$185 \quad R(\lambda) = 1 - d \times \left(\frac{I_{N_2}(\lambda) \times n_{N_2} \times \sigma_{Rayl,N_2}(\lambda) - I_{He}(\lambda) \times n_{He} \times \sigma_{Rayl,He}(\lambda)}{I_{He}(\lambda) - I_{N_2}(\lambda)} \right) \quad (2)$$

186 Where d is the distance between two high-reflectivity mirrors, λ is the wavelength, $I_{N_2}(\lambda)$ and $I_{He}(\lambda)$ are spectrums
 187 obtained when the cavity is filled with pure N₂ and He, respectively, n_{N_2} and n_{He} are the number density calculated
 188 at measurement temperature and pressure in the cavity, respectively, $\sigma_{Rayl,N_2}(\lambda)$ and $\sigma_{Rayl,He}(\lambda)$ are the Rayleigh
 189 scattering section of N₂ and He, respectively (Shardanand, 1977; Snee and Ubachs, 2005). Fig. 2 shows the average
 190 of mirror reflectivity calibration results. The $R(\lambda)$ is above 0.9999 in 435-465 nm, and up to 0.99992 at 450 nm. The
 191 total uncertainty of the mirror reflectivity is 5%, which comes from the uncertainty in the scattering section of N₂.
 192 The blue line is the average optical path length when the sampling flow rate in the cavity is 0.8 L min⁻¹, which is
 193 equal to $d_{eff}/(1-R)$ (d_{eff} is 31.84 cm), with the value up to 5.2 km at 450 nm.

194



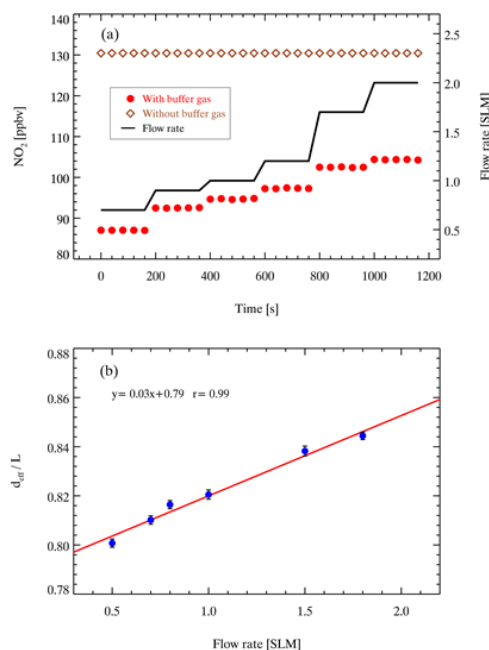
195
 196 Figure 2. Mirror reflectivity and optical path length calibrated by He (>0.99999) and N₂ (>0.99999). The red line is the average $R(\lambda)$,
 197 and the blue line is the optical path length.

198 3.2 Effective cavity length

199 The effective length of absorbers (named effective cavity length, d_{eff}) in the detection cell is shorter than the physical
 200 distance of the cavity; thus, it needs to be calibrated. We performed the concentration determination on the NO₂
 201 standard source (130 ppbv) under two experimental settings with or without purging and then used Eq. 1 to calculate
 202 d_{eff} . The ratio of NO₂ absorption with and without purging is equal to the ratio of the effective cavity length to the
 203 physical distance L between the mirrors (d_{eff}/L). NO₂ stand was prepared from a bottled standard (5 ppmv NO₂) and
 204 diluted with high-purity N₂ in the multi-gas calibrator (146i, Thermo Fisher Scientific Inc., Waltham, MA, USA). As
 205 shown in Fig. 3a, the retrieved concentration of NO₂ shows a positive correlation trend with the flow rate with N₂
 206 purging; the concentration of NO₂ is 130 ppbv without a purge. The d_{eff}/L at different sampling flow rates is shown
 207 in Fig. 3b. It is found that the ratio of the effective cavity length increases as the flow rate increases, suggesting the
 208 importance of airflow rate stability during sampling. The uncertainty of the prepared NO₂ standard source is estimated
 209 to be 2.0%, while the uncertainty of the NO₂ absorption cross-section is 4.0%, according to Voigt et al. (2002). As a
 210 result, the total uncertainty of d_{eff} calibration is 4.5% (Voigt et al., 2002).



211



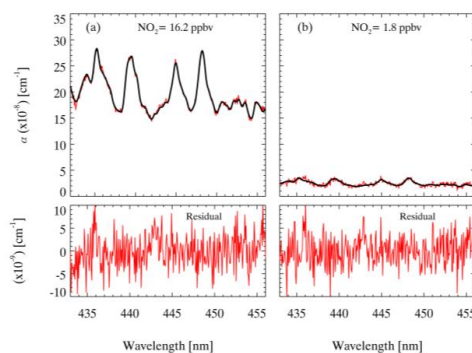
212
213 Figure 3. The results of the effective cavity length. (a) The black line represents the flow rate, the red points, and brown diamonds
214 represent the retrieved NO₂ concentration with and without nitrogen purge (100 sccm×2), respectively; (b) The correlation dependence
215 of the ratio of the effective cavity length (d_{eff}) to cavity physical distance (L) on the sampling flow rate.

216 3.3 Spectral fitting

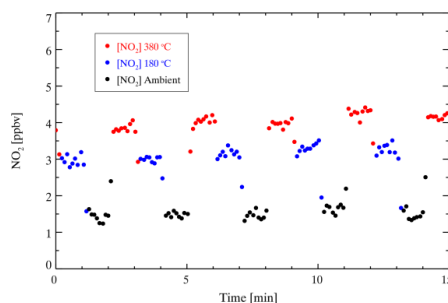
217 The absorption cross-section of NO₂ measured by (Voigt et al., 2002) is used to retrieve NO₂ concentration in this
218 study. The absorption cross-section of NO₂ between 435-455nm is selected to perform the spectral fitting. It was
219 reported that the NO₂ cross-section is not sensitive to the temperature change (Vandaele et al., 2002; Voigt et al.,
220 2002), so the convolution is only performed for our instrument setup at ambient temperature. The peak at 436.2 nm
221 of Hg spectrum measured by the spectrometer is used to generate a wavelength-dependent instrument slit function
222 that accounts for the change of spectral resolution over the CCD pixels. The convoluted cross-section of NO₂ is
223 shown in Fig. S1. The measured absorption coefficient (α) is processed by DOASIS (Differential Optical Absorption
224 Spectroscopy Intelligent System). The fitting shift is constrained within ± 0.2 nm. Glyoxal has strong absorption in
225 the same optical window (Liu et al., 2019; Min et al., 2016; Thalman et al., 2015; Thalman and Volkamer, 2010;
226 Washenfelder et al., 2008), but here we do not take into consideration in spectrum fitting. Fig. 4 shows two examples
227 of the spectral fitting of measured absorption of high and low NO₂ at 6 s integration time during the ambient
228 measurement. The retrieved mixing ratio of NO₂ is 18.2 ppbv and 1.8 ppbv, respectively. The corresponding fitting
229 residual is in the range of 10×10^{-9} at 435-455 nm, suggesting the system can guarantee the accuracy for different
230 levels of NO₂ measurement. A typical measurement sequence during the ambient measurement is illustrated in Fig.
231 5, which displays NO₂ mixing ratios after three channels alternatively. The mixing ratio of NO₂ in different channels
232 is detected periodically, and there are several transitional points due to switching measurement phases. As we discuss
233 later, the mixing ratio of ANs and PNs can be calculated by subtracting the NO₂ mixing ratio measured from different



234 channels.
 235



236
 237 Figure 4. An example of the spectral fit for an extinction spectrum measured (6 s average) during field measurements. The fitted results
 238 of NO₂ are shown and the total fit result, and the residual at high concentration (a) and low concentration (b).



239
 240 Figure 5. An example of typical measurements performed in a field study with 6 s spectrum integral time. A measurement cycle includes
 241 three phases whose duration is 60 s. The red points denote the NO₂ mixing ratio measured in the ANs channel ([NO₂] 380°C), the blue
 242 ones denote the NO₂ mixing ratio measured in the PNs channel ([NO₂] 180°C), and the black ones denote the NO₂ mixing ratio measured
 243 in the reference channel ([NO₂] Ambient).

244
 245 There are two methods to determine the mixing ratio of ONs and PN_s. One is the differential concentration method.
 246 The differential NO₂ concentration is gradient subtracted between different measurement channels after the spectrum
 247 fitting, as shown in Eqs. 3-6, and the I_0 is fixed during the data analysis by using pure nitrogen spectrum ('CONC'):
 248 I_{TD380} and I_{TD180} are spectrums obtained by ONs and PN_s measurement channels, respectively; I_{N_2} is a spectrum
 249 obtained when the cavity is filled with N₂ (>0.999999); α_{TD380} and α_{TD180} are absorption coefficients when I_{N_2} is
 250 set as the reference spectrum, and I_{TD380} or I_{TD180} is set as sample spectrum, respectively; after eliminating the
 251 abnormal points caused by switching, [ON_s] is obtained by subtracting the average of the effective points of
 252 [NO₂]_{TD380} and [NO₂]_{REF}, and [PN_s] is obtained by subtracting the average of the effective points of [NO₂]_{TD180} and
 253 [NO₂]_{REF}. The other method is the differential absorption method, by using the dynamic background spectrum
 254 method ('SEPC') for spectral fitting (Eqs.7-8): I_{REF} is the spectrum obtained at the ambient temperature
 255 measurement channel; ON_s can be retrieved based on I_{TD380} and I_{REF} ; PN_s can be retrieved by I_{TD180} and I_{REF} .

256 An intercomparison of field measurement shows that the 'SEPC' method results in fewer outliers (Fig. 6). For the
 257 'SEPC' method, the shift and squeeze of the spectrum is performed only once during the spectrum fitting, which
 258 reduces the uncertainty caused by the second spectrum fitting. Therefore, we selected the 'SEPC' method to retrieve



259 the concentration of NO₂, PNs, and ANs in the following data processes.

$$260 \quad \alpha_{TD380} = \left(\frac{I_{TD380}}{I_{N_2}} - 1 \right) \left(\frac{1-R(\lambda)}{d_{eff}} \right) \quad (3)$$

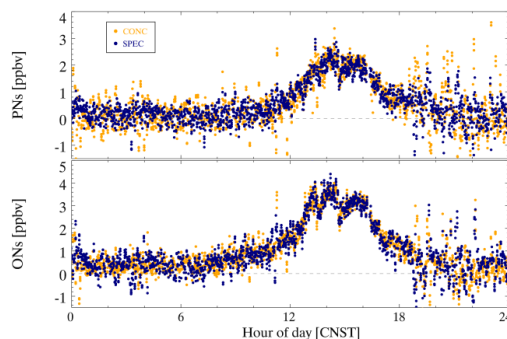
$$261 \quad \alpha_{TD180} = \left(\frac{I_{TD180}}{I_{N_2}} - 1 \right) \left(\frac{1-R(\lambda)}{d_{eff}} \right) \quad (4)$$

$$262 \quad [ONS] = [NO_2]_{TD380} - [NO_2]_{REF} \quad (5)$$

$$263 \quad [PNs] = [NO_2]_{TD180} - [NO_2]_{REF} \quad (6)$$

$$264 \quad \alpha_{[ONS]} = \left(\frac{I_{TD380}}{I_{REF}} - 1 \right) \left(\frac{1-R(\lambda)}{d_{eff}} \right) \quad (7)$$

$$265 \quad \alpha_{[PNs]} = \left(\frac{I_{TD180}}{I_{REF}} - 1 \right) \left(\frac{1-R(\lambda)}{d_{eff}} \right) \quad (8)$$



266
 267 Figure 6. An example of the calculation results of the fixed I_0 ('CONC') and dynamic I_0 ('SPEC') methods performed in the field
 268 measurements. Orange dots represent the results of the 'CONC' method, and dark blue dots represent the calculation results of the 'SPEC'
 269 method.

270 3.4 The efficiency of thermal dissociation

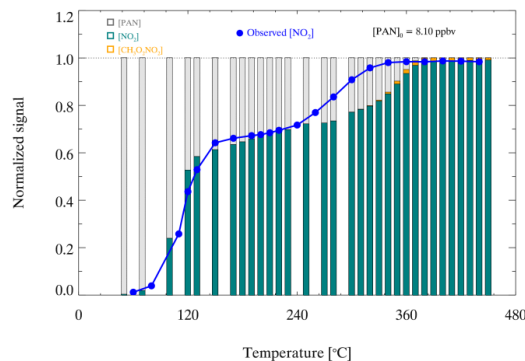
271 The strength of the bond between the NO₂ group and the organic group determines the temperature to pyrolyze the
 272 organic nitrates. The cleavage of the NO₂ group in PNs requires about 85-115 kJ/mol (Kirchner et al., 1999), while
 273 for ANs, the pyrolysis process requires about 160-170 kJ/mol (Roberts, 1990), so PNs are more prone to dissociate
 274 thermally. For the pyrolysis measurement of organic nitrates, the exact temperature setting for complete pyrolysis
 275 varies, mainly due to the many factors that affect the efficiency of thermal dissociation, such as the specificity of the
 276 quartz tube, the heating residence time, and temperature distribution of the heating part (Womack et al., 2017). The
 277 thermal dissociation of PAN was tested separately in the PNs and ANs channels, and the efficiency curves are the
 278 same between ANs channel and PNs channel. The heating temperature is the temperature of the quartz tube surface
 279 rather than the airflow temperature in the quartz tube. The experiments were done under normal sampling conditions,
 280 and the heating temperature was evaluated from room temperature to 440 °C to determine the appropriate heating
 281 temperature. Fig. 7 shows the pyrolysis of PAN start when the heating temperature is about 50 °C. The curve seems
 282 to reach a platform when the heating temperature is around 180 °C. However, the normalized signal of thermal
 283 dissociation of PAN reaches the final platform once the temperature is above 360 °C. Similarly, the PAN is reported
 284 thermally dissociated totally about 400 °C (Friedrich et al., 2020). The occurrence of the dual-platform phenomenon
 285 is due to the competitive progress of pyrolysis and recombination reactions. PAN will produce NO₂ and PA after
 286 thermal dissociation, but PA will recombine with NO₂ if PA is not lost on the wall surface in time (R7-R8). Therefore,
 287 the thermal curve shows two platforms as the heating temperature increases.



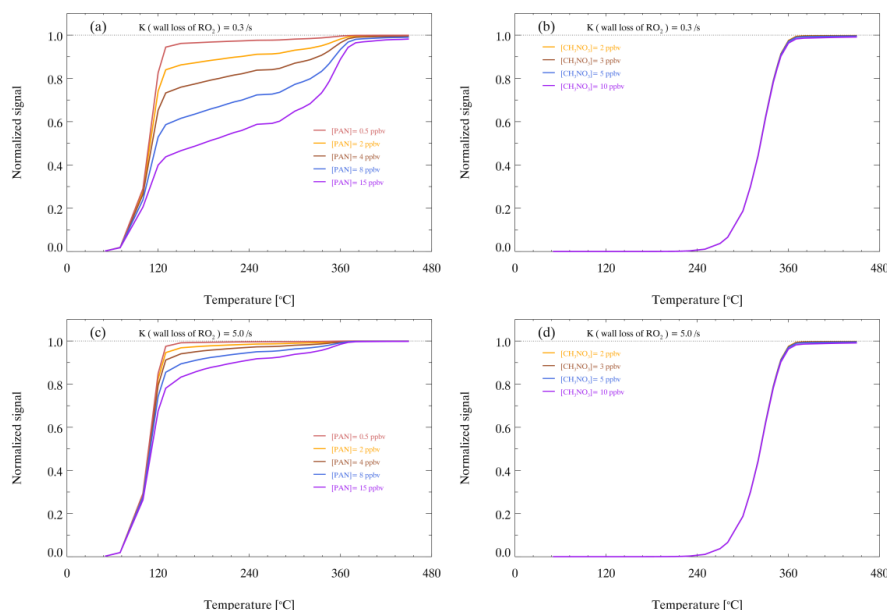
288 To further study the thermal dissociation of organic nitrates in the heated channels, the box model simulations are
289 conducted to reproduce the response relationship between heating temperature and NO_2 generated by pyrolysis. As
290 shown in Fig. 7, PAN gradually transforms into NO_2 and $\text{CH}_3\text{O}_2\text{NO}_2$ as the setting temperature increases. The
291 simulated signals of thermal dissociation of PAN show two platforms similar to the experimental results generally.
292 However, there are some differences between 260 to 360 °C, which may come from the simulation uncertainties such
293 as the temperature profile in the heating channel, the follow-up reactions of PA radicals and their reaction rates. The
294 first platform at 180 °C is caused by the recombination of PA and NO_2 after the pyrolysis of PAN, so the recombination
295 cannot be ignored when the heating temperature level is around the first platform. The second temperature platform
296 period indicates that almost all PAN is transformed into NO_2 , which is due to the increase in the pyrolysis loss of PA
297 and the pyrolysis of PAN enhanced with the temperature increases. The concentration of PAN source and wall loss
298 rate of RO_2 influence the fraction of related species. Fig. 8(a) and (c) show that the gap between the two platforms
299 increases with PAN concentration and decreases with the wall loss rate coefficients of RO_2 increasing. The wall loss
300 of RO_2 competes with the recombination of PA radical and NO_2 . Therefore high wall loss rate coefficient of RO_2
301 reduces the recombination for PAN.

302 The consistent between observed and simulated thermal efficiency of PAN suggests that the model simulation is
303 reliable. Without the ANs source to quantify the thermal efficiency of ANs, we try to use the model simulation to
304 determine the heating temperature of the ANs channel. Based on the same parameter settings of the model, MeN
305 (methyl nitrate, CH_3NO_3) is selected as the representative of ANs to simulate the pyrolysis efficiency curve. Fig. 8(b)
306 and (d) show that the MeN can be thermally dissociated totally when the temperature over 380 °C, indicates that the
307 temperature set to 380 °C for ANs channel is reasonable. The simulation also showed that the two factors have almost
308 no effect on the pyrolysis of MeN, which is completely pyrolyzed to produce NO_2 when the temperature is 380 °C.
309 The simulation results are similar to previous reports about the thermal dissociation of ANs, whose heating
310 temperatures are set in the range from 350 to 450 °C (Day et al., 2002; Sadanaga et al., 2016; Sobanski et al., 2016;
311 Thieser et al., 2016). Therefore, 180 °C and 380 °C are selected as the heating temperature of the PNs channel and
312 ANs channel, respectively.

313
314



315
316 Figure 7. Normalized signals of thermal dissociation of PAN. The blue points represent the normalized signal of the observed NO_2
317 mixing ratio during thermal dissociation. The histogram represents the simulated distribution of thermal dissociation products at different
318 temperatures, in which the gray, green and orange columns represent PAN, NO_2 and HNO_3 , respectively.
319



320

321 Figure 8. Model simulated thermal decomposition profiles of PAN and MeN with different amounts of PAN or MeN under different wall
322 loss rate coefficient of RO_2 . Panel (a) and (b) show that the NO_2 signal of PAN and MeN when the wall loss rate coefficient of RO_2 is
323 $0.3 /s$. Panel (c) and (d) show that the NO_2 signal of PAN and MeN when the wall loss rate coefficient of RO_2 is $5 /s$.

324 4. Results and discussion

325 4.1 Measurement interference

326 Previous studies have shown that the filter losses and wall losses of NO_2 , PNs and ANs are small (Paul et al., 2009;
327 Thieser et al., 2016). As shown in Fig. S2, the response to concentration changes of PAN was nearly instantaneous
328 under the normal sampling, suggesting the memory effects on the inlet and cavity tubing are insignificant. As shown
329 in Fig. S3 and Fig. S4, the filter loss and sampling tube are negligible. The transmission efficiency for PAN is $> 97\%$
330 if there is a fresh filter membrane in the holder. We purpose that changing the filter once a day can ensure a high
331 transmission efficiency of the species to be detected. In the heating channels, organic nitrates will be thermally
332 dissociated to produce NO_2 , but some simultaneous reactions will affect the NO_2 mixing ratio. The potential
333 interferences mainly come from the following reactions: formation NO_2 via NO and O_3 , pyrolysis of O_3 , reactions of
334 organic radicals with NO and NO_2 , pyrolysis of other reactive nitrogen oxides.

335 The formation of NO_2 in a dark reaction between NO and O_3 should be considered in NO_2 measurement. If the
336 reaction has continued for a certain time (t) during the sampling, the amount of NO_2 formed $[NO_2]t$ can be calculated:
337 $[NO_2]t = k \times [NO] \times [O_3] \times t$, where k is the rate coefficient for Reaction (R4) and is given as $2.07 \times 10^{-12} \exp(-$
338 $1400/T) \text{ cm}^3/\text{molecule/s}$ (Atkinson et al., 2004). According to the temperature distribution and the airflow
339 temperature measurements changing with the distance after the heating quartz tube, the heated channel temperature
340 profiles under normal sampling are shown in Fig. S5. Based on the temperature profile, the reaction of NO and O_3
341 in the three channels can be calculated. As the residence time of airflow in three channels is short and similar (0.806 s
342 in reference channel; 0.697 s in ANs channel; 0.730 s in PNs channel), the results of simulations show the inference
343 is small. For example, in a case on an ozone pollution day with $O_3 = 100 \text{ ppbv}$, $NO = 2 \text{ ppbv}$ and $NO_2 = 5 \text{ ppbv}$, the
344 NO_2 produced by the reaction of NO and O_3 in the reference channel is 0.07 ppbv , corresponding to 1.3% of



345 atmospheric NO₂. Similarly, the interferences in ANs channel and PNs channel are 0.14 ppbv (2.7% of NO₂) and
 346 0.10 ppbv (2.0% of NO₂), respectively.

347 The thermal degradation of O₃ occurs at high temperatures, which reduces NO₂ to NO via O(³P) (R5-R7). The
 348 interference was once ignored in the process of PNs and ANs pyrolysis (Day et al., 2002). However, the subsequent
 349 studies have shown that the reaction can cause significant negative deviations in the measurements of NO₂ under
 350 higher temperature, and the degree of interference is closely related to the temperature change of the pyrolysis module
 351 (Lee et al., 2014; Thieser et al., 2016). To determine the reduction reaction effect, we did the experiments in which
 352 NO₂ was detected in three different channels when the various NO₂ and O₃ were added. The experiment results are
 353 shown in Table 1 with various amounts of NO₂, and O₃ added. No significant NO₂ mixing ratio difference was
 354 observed between the reference and ANs channels. We showed a negligible interference here, which is different from
 355 previous reports (Lee et al., 2014; Thieser et al., 2016). This is likely caused by a much lower temperature setting of
 356 our ANs measurement channel. Since the pyrolysis rate constant of O₃ is highly temperature-dependent, the lower
 357 temperature would largely reduce the level of O atom as well as this interference.



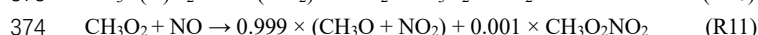
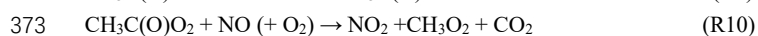
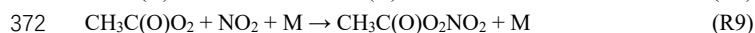
362

363 Table 1. The measurements of NO₂ mixing ratio in three channels of TD-CEAS with different added amounts of NO₂ and O₃.

Order	[NO ₂] [ppbv]	[O ₃] [ppbv]	[O ₃]×[NO ₂] [ppbv×ppbv]	[NO ₂] _{TD380} [ppbv]	[NO ₂]-[NO ₂] _{TD380} [ppbv]
0	7.45±0.27	48.19	359	7.79±0.27	-0.34
1	7.89±0.27	67.47	532	8.17±0.28	-0.28
2	15.58±0.29	48.19	751	15.84±0.28	-0.26
3	8.23±0.27	96.38	793	8.22±0.28	0.01
4	15.77±0.25	67.47	1064	15.94±0.27	-0.17
5	8.43±0.27	144.57	1218	8.64±0.28	-0.21
6	16.18±0.28	96.38	1559	16.20±0.28	-0.02
7	16.28±0.30	144.57	2354	16.26±0.31	0.02

364

365 The RO₂ recombines with NO₂ or reacts with NO interfere with the measurement of ANs and PNs. Taking PAN
 366 as an example, the organic radicals may trigger interference as described above (R8-R15). The PA produced after
 367 thermal dissociation of PAN (R8) can recombine with NO₂ (R9). RO₂ can oxidize NO to produce NO₂ while
 368 generating another organic radical (R10). CH₃O₂ can further initiate a series of reactions that affect the distribution
 369 of NO₂ (R11-R15). Therefore, the lifetime and fate of PA generated by PAN pyrolysis will cause the interference,
 370 and atmospheric NO and NO₂ will affect the degree of measurement interference.

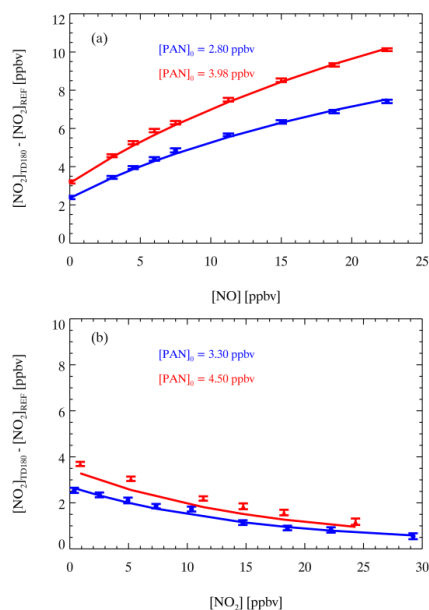




380 A set of laboratory experiments was conducted to measure the interference in the PNs channel with different NO,
381 NO₂ and PAN levels. Fig. 9a shows the measurement and simulation results of different PAN concentration mixed
382 with different concentrations of NO. With the increase in NO added, the detected PNs mixing ratio (the signal
383 difference between PNs channel and REF channel) also gradually increased. More NO reacted with PA radicals
384 generated during thermal dissociation to produce additional NO₂ within the residence time in the PNs channel, which
385 led to the measurements higher than the PAN source level. In contrast, as shown in Fig. 9b, the measured PNs were
386 lower than PAN source level when NO₂ was added to the source, and the bias increased with the increase of NO₂
387 added. The addition of NO₂ in the system improves the overall concentration of NO₂ in the PNs channel, promoting
388 the reformation to PAN.

389 We conducted numerical simulations by a box model to mimic the observation and check the chemical reactions
390 in the PNs channel. Fig. 9a shows the simulations have a good consistency with the experiment result under different
391 NO levels. Fig. 9b shows that the model can capture the trend of experimental results on NO₂ interferences, except
392 the case of PAN source of 4.5 ppbv, which might due to reaction of small excess RO₂ in the PAN source line and
393 extra NO₂ added to generate additional PAN before sampling into the instrument. Overall, these experiments proved
394 that NO and NO₂ interfere with the measurement of PNs. However, the agreement of experiments and model results
395 indicates that the interference of NO, NO₂ for PNs measurements can be corrected. In the field measurements, the
396 correction factor refers to the ratio between the real value and the measured value of PNs. For example, in a typical
397 case during field measurements where PAN = 3 ppbv, NO = 8 ppbv and NO₂ = 5 ppbv, the difference between PNs
398 channel and reference channel is equal 4.54 ppbv (equivalent to the measured PAN), which require a correction factor
399 of 0.66. Here, nearly 40000 simulations are done under various initial concentrations of NO (0-70 ppbv), NO₂ (0-60
400 ppbv) and PAN (0-10 ppbv) to get the correction factor look-up table for our first field measurement (detailed in Sect.
401 4.3). The correction factor for PNs measurements can be determined by the look-up table according to the
402 atmospheric NO and NO₂ and the raw data of PNs measurements with linear interpolation.

403



404



405 Figure 9. Modeled (lines) and measured (points) difference between the NO₂ signal in the PNs channel and reference channel for different
406 PAN samples with different added amounts of NO (a) and NO₂ (b). The error bars show one standard deviation.

407 Fig. 10 displays the interference of NO and NO₂ to the PAN measurements in the ANs channel. The thermal
408 dissociation of PA radical is rapid, and the reformation of PAN is also suppressed at higher temperatures. So, the
409 PAN measurement response to NO and NO₂ added are weakened. The laboratory experiments showed that the
410 measured signal difference increased with NO (Fig. 10a). Hence, the presence of NO still led to the higher
411 measurement result of ONs than the source value. However, the interference was weakened compared with the
412 measured results in the PNs channel at the same NO and PAN source level (Fig. 9a). Similarly, the experiments with
413 NO₂ added showed the underestimated measurements of ONs, and the interference was significantly weakened
414 compared with that in the PNs channel. We used the same box model except updating the temperature distribution
415 and the corresponding residence time in the ANs tube to simulate the interference of NO or NO₂ under different PAN
416 source levels. However, there are still some uncertainties about the reaction mechanism and reaction rate for the
417 thermal dissociation of PAN at such high temperatures. Similar to the simulation results of (Thieser et al., 2016), we
418 did the sensitivity tests about the follow-up reactions of PA, and found that the isomerization of PA to CH₂C(O)OOH
419 has a great effect on the consistency of the experiments and the simulation results. If the reaction rate of the branching
420 reaction is set to zero, as shown in Fig. 10, the simulation results capture the trend well when NO₂ or NO is added.
421 Many factors affect the signal of NO₂ produced by the thermal dissociation of PAN, so the mechanism scheme
422 mentioned above provides a reasonable assumption to the interference process. Overall, the box model predicts the
423 interference of PAN measurement caused by NO and NO₂. Therefore, the correction factors of different cases under
424 various NO, NO₂ and PAN added are simulated to form the second look-up table, and then we can capture the signal
425 contribution of PNs to the ONs measurements in ANs channel.

426 MeN is pyrolyzed to produce NO₂ and CH₃O in the ANs channel (R16), and CH₃O is an important intermediate
427 product of the reactions about PA (R10 - R12). Therefore, the mechanism scheme about PAN applies to simulations
428 to correct the interference of atmospheric NO_x to the ANs measurements. Similarly, the different cases under various
429 NO, NO₂ and MeN added were simulated to form the third look-up table for the corrections of ANs measurements
430 in the ANs channel. Through the look-up tables, the method to correct ANs measurements are established. Based on
431 the 'SEPC' method, the raw concentration of ONs ([ONs]) and PNs ([PNs₁₈₀]) can be gained, which need further
432 corrections. As for PNs measurements, the related cases can be found by the atmospheric NO_x and the detected
433 [PNs₁₈₀] in PNs channel according to the first look-up table. Then the right correction factor (*C1*) is calculated
434 based on linear interpolation between the correction factor and detected signal of PAN measurement under the same
435 NO_x distribution. As shown in Eq. 9, the corrected PNs mixing ratio ([PNs_C]) is derived by [PNs₁₈₀] and *C1*. The
436 interference relationships between atmospheric NO_x and PNs are different in two TD channels, so it is necessary to
437 determine the contribution of PNs to ONs signal before subtracted in the ANs channel. We use the [PNs_C] derived
438 by the first look-up table and the atmospheric NO_x to determine the correction factor (*C2*) for PNs signal based on
439 the second look-up table. Then the contribution of PNs to ONs measurements ([PNs₃₈₀]) is determined by Eq. 10.
440 Therefore, the raw concentration of ANs ([ANs]) is calculated by subtracting [PNs₃₈₀] from [ONs] (Eq. 11). As
441 for the correction of ANs, the correction factor (*C3*) is determined by the third look-up table, and then the result is
442 multiplied [ANs] to obtain the corrected ANs mixing ratio ([ANs_C]) (Eq. 12).

$$443 \quad [\text{PNs}_C] = [\text{PNs}_{180}] \times C1 \quad (9)$$

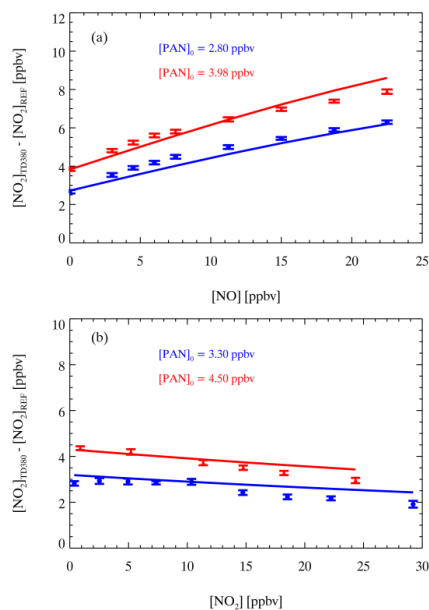
$$444 \quad [\text{PNs}_{380}] = \frac{[\text{PNs}_C]}{C2} \quad (10)$$

$$445 \quad [\text{ANs}] = [\text{ONs}] - [\text{PNs}_{380}] \quad (11)$$

$$446 \quad [\text{ANs}_C] = [\text{ANs}] \times C3 \quad (12)$$



447 In addition to the interference mentioned above, other nitrogen compounds may undergo pyrolysis to generate NO_2
448 in the heating channels, such as N_2O_5 and ClNO_2 (Li et al., 2018; Wang et al., 2017a; Womack et al., 2017), which
449 may be a source of uncertainty for measurements of organic nitrates. These interferences can be extracted with the
450 simultaneous measurement of N_2O_5 and ClNO_2 .
451



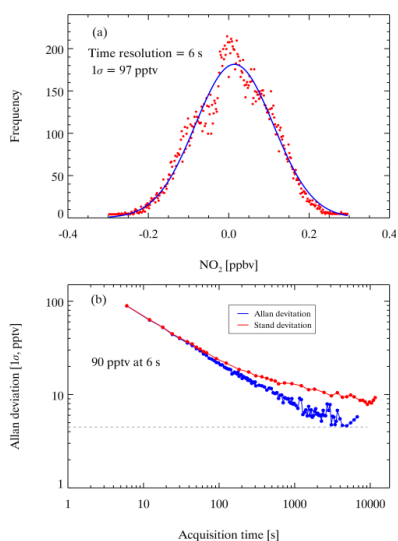
452
453 Figure 10. Modeled (lines) and measured (points) difference between the NO_2 signal in the ANs channel and reference channel for
454 different PAN sources with different amounts of NO (a) and NO_2 (b). The error bars show one standard deviation.

455 4.2 Uncertainty and detection limit

456 The uncertainty of CEAS measurement of NO_2 is contributed by absorption cross-section, mirror reflectivity, and
457 effective cavity length. The absorption cross-section of NO_2 is taken from Voigt et al. (2002), whose uncertainty is
458 about 4% (Voigt et al., 2002); the uncertainty of mirror reflectivity is about 5%, determined by the error of the
459 scattering cross-section of N_2 ; the uncertainty of effective cavity length is about 4.5%. According to the Gaussian
460 error propagation, the associated uncertainty of the ambient NO_2 measurement is $\pm 8\%$ based on the above parameters.
461 The precision of the instrument can be assessed by the Allan deviation and standard deviation. We continuously
462 measured 21077 spectrums when the cavity was filled with N_2 under purge. The integration time was 3 s and the
463 sampling time was 6 s as every two spectra average before saving. The first 100 nitrogen spectrums collected were
464 averaged as I_0 , and all the spectrums were analyzed based on the I_0 . The data set was divided into 300 gradients for
465 Gaussian fitting, and 1σ is 97 pptv, as shown in Fig. 9a. The 21077 spectrums were averaged at different time intervals
466 (from 6 s to 11400 s). The Allan deviations at different time intervals were calculated (Duan et al., 2018; Langridge
467 et al., 2008; Wang et al., 2017a). As shown in Fig. 9b, the Allan deviation decreases as sampling time increases when
468 the sampling time is smaller than 1300 s, and the minimum is 5 pptv. When the sampling time is 6 s, the Allan
469 variance can reach 90 pptv, close to 1σ . ANs and PNs are detected by the same CEAS system and calculated by the
470 dynamic I_0 ('SEPC') method, so their precision is identical with NO_2 measurement. The uncertainty of [ANs] and
471 [PNs] mainly comes from the spectrum fitting to derive the concentration of NO_2 and the interference correction in



472 heated channels, which should be larger than 8%.
473



474
475 Figure 11. The instrument performance with different integration times. (a) the standard deviation of the measurements of NO₂ for a 6 s
476 integration time. (b) Allan deviation plots for measurements of NO₂ for a 6 s integration time.

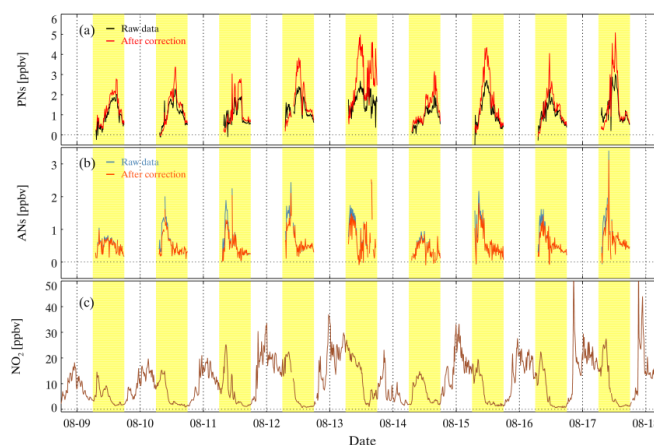
477 4.3 The performance in field observation

478 TD-CEAS has deployed the first field observation in Xinjin County, Chengdu, China, in 2019, referred to as the
479 CHOOSE campaign (Yang et al., 2020). As shown in Fig. S6, there is a residential area at 5 km from the northwest
480 of the site; the surrounding area is lush with trees and is close to a forest park and a national wetland park; there is
481 an industrial park at about 12 km to the west and 8 km to the south separately. During the CHOOSE campaign, TD-
482 CEAS was deployed in a container. The sampling inlet protruded from the container top and was supported by a
483 bracket, with a height of 4 m above the ground. We determined the raw data of PNs and ONs during the observation
484 period. Base on the NO, NO₂, and raw PNs measured simultaneously, the specific correction factor picked from look-
485 up table can be referred to, and then the raw data is corrected. The raw concentration of ANs can be obtained by
486 subtracting the simulated PNs based on the second look-up table from the measured ONs in the ANs channel, and
487 then the raw ANs are corrected according to the third look-up table. Fig. 12a shows the time series of raw data and
488 the corrected data of PNs from August 9th to August 18th during the CHOOSE campaign, and Fig. 12b shows the time
489 series of ANs measurements before and after corrected. The correction factors used during corrections are shown in
490 Fig. S7. The value of *C1* is generally greater than 1.0 (except during the morning), suggesting the role of NO₂ is more
491 significant than NO in this site. The tendency of *C2* and *C3* is similar to *C1* during measurements, but the daily
492 change of *C2* and *C3* relatively smaller as the decrease of the sensitivity of interferences in ANs channel as mentioned
493 above. Fig. 12c shows that NO₂ was constantly increasing at night, reaching a peak near the early morning, and
494 maintaining a high value around 11 a.m. High mixing ratios of PNs were observed during the measurement, and the
495 diurnal variation of PNs was clear. The peak of ANs appeared in the noontime and several hours before that of PNs.

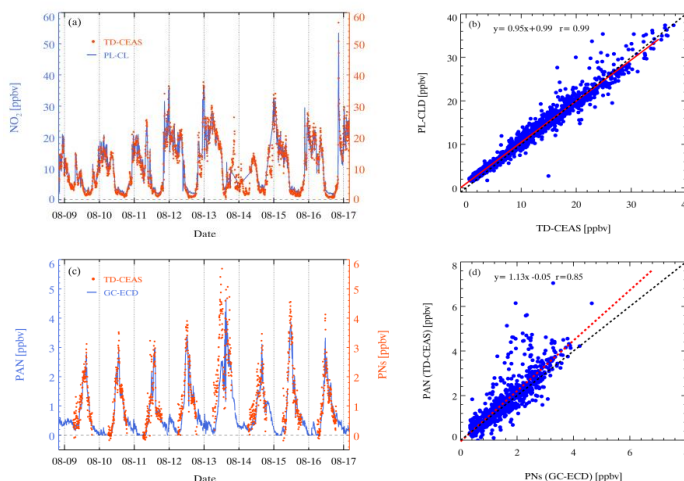
496 A photolytic conversion chemiluminescence detector (PC-CLD) was used to measure NO and NO₂ in the campaign.
497 The time series of NO₂ measured by TD-CEAS and PL-CLD with 5 min average is shown in Fig. 13a, which are
498 from August 9th to August 16th. The trend of NO₂ measured by two instruments agree well, but the results of PL-CLD



499 are higher when the mixing ratio of NO_2 is low at noon. Fig. 13b shows that the correlation coefficient of the NO_2
500 concentration measured by two instruments is up to 0.99. The results of TD-CEAS is a little higher than the results
501 of PL-CLD as the slope is 0.95, which is reasonable when considering the instrument uncertainties. The time series
502 of PNs (TD-CEAS) and PAN (GC-ECD) is shown in Fig. 13c, and the trends are relatively consistent, but the results
503 of PNs are higher than the results of PANs measured by GC-ECD, especially in the noontime. The result is reasonable
504 since the PAN is the most but not equal to the total PNs. The correlation between the two instruments is good as the
505 correction coefficient is up to 0.85 (Fig. 13d), suggesting our instrument's feasibility in PNs measurement.
506



507
508 Figure 12. Time series of the observed mixing ratios of PNs, ANs and NO_2 , during ozone pollution from the CHOOSE campaign in
509 2019. The yellow regions indicate the period for the daytime. (a) The black lines represent the raw measurements of PNs, and the red
510 lines are the corrected measurements of PNs according to the lookup table. (b) The blue lines represent the raw measurements of ANs,
511 and the orange lines are the corrected measurements of ANs according to the lookup tables. (c) The measurements of NO_2 in the reference
512 channel.
513



514



515 Figure 13. Comparison of TD-CEAS and PL-CLD in the CHOOSE campaign: Panel (a) shows the time series of NO₂ measurements.
516 Orange points represent the results of TD-CEAS, and blue line represents the results of PL-CLD. Panel (b) shows the NO₂ correlation
517 between the two instruments. Comparison of the PNs measured by TD-CEAS and the PAN measured by GC-ECD: Panel (c) shows the
518 time series of PNs and PAN, orange dots represent the results of TD-CEAS, and blue line represents the results of GC-ECD; Panel (d)
519 shows the PNs correlation of the two instruments.

520 5. Conclusions and outlook

521 We developed a new TD-CEAS instrument to measure PNs, ANs and NO₂ in the atmosphere. The instrument uses
522 only one CEAS to measure NO₂, PNs and ANs to avoid the error caused by different detectors. This TD-CEAS is a
523 combination of CEAS and pyrolysis technology for organic nitrates measurement. CEAS uses the small cavity cell
524 of the cage system, with a total length of about 60 cm, a small overall volume and low energy consumption. The use
525 of a NO₂-CEAS system to detect three classes of compounds reduces the instrument uncertainty. The short cycle
526 period meets the atmospheric lifetime requirements of organic nitrates for measurement time resolution in general.
527 The time resolution of the instrument is 6 s, one measurement cycle is 3 min, and sample gas from each channel is
528 measured for 1 min. The instrument has a lower detection limit of 97 pptv (1 σ). The interferences in the heating
529 channels are characterized under different levels of ambient NO, NO₂ and ONs (PAN or MeN) by laboratory
530 experiments and model simulations. Three look-up tables were established to correct the PNs and ANs concentration
531 based on the detected NO_x and organic nitrates.

532 The instrument was deployed in field measurement in Chengdu, China, and the PNs measured by TD-CEAS
533 showed a good consistency with PAN measured by GC-ECD during the daytime. However, when the ambient NO₂
534 in the sampled air masses change drastically, the difference in NO₂ between adjacent measurement modes in a cycle
535 will be erroneous, resulting in the unfeasible measurement (Fig. S8). The simultaneous measurements show that the
536 N₂O₅ mixing ratio during nighttime is low and zero during the daytime. Therefore, the interferences of the N₂O₅ is
537 negligible for the ONs measurements during the day for the CHOOSE campaign. Nevertheless, the observed ANs
538 may be subject to the level of ClNO₂ without the simultaneous ClNO₂ measurement. Overall, this instrument is very
539 suitable for detecting NO₂, PNs, and ANs in the chamber studies or ambient measurements with relatively stable air
540 masses free of intensive emission interferences. Multiple detectors can be used for simultaneous observation to avoid
541 limited measurement conditions. More importantly, the ways to reduce the impact of interference reaction in heated
542 channels shall be investigated, such as improving the wall loss of RO₂ through increasing surface areas of the
543 sampling lines or reducing the residence time during the sampling.

544

545 **Data availability.** The datasets used in this study are available from the corresponding author upon request
546 (k.lu@pku.edu.cn).

547

548 **Author contributions.** K.D.L. and H.C.W. designed the study. C.M.L, H.C.W. set up and characterized the
549 instrument, analyzed the data and wrote the paper with the input of K.D.L. All authors contributed to the field
550 measurements, discussed and improved the paper.

551

552 **Competing interests.** The authors declare that they have no conflict of interest.

553

554 **Acknowledgments.** This work was supported by the National Natural Science Foundation of China (Grants No.
555 21976006); the National Research Program for Key Issue in Air Pollution Control (Grants No. DQGG0103-01);
556 Beijing Municipal Natural Science Foundation for Distinguished Young Scholars (Grants No. JQ19031).

557

558



559 **References.**

- 560 Arey, J., Aschmann, S. M., Kwok, E. S. C., and Atkinson, R.: Alkyl nitrate, hydroxyalkyl nitrate, and hydroxycarbonyl formation from
561 the NO_x-air photooxidations of C-5-C-8 n-alkanes, *J. Phys. Chem. A*, 105, 1020-1027, 2001.
- 562 Atkinson, R., Baulch, D. L., Cox, R. A., Crowley, J. N., Hampson, R. F., Hynes, R. G., Jenkin, M. E., Rossi, M. J., and Troe, J.: Evaluated
563 kinetic and photochemical data for atmospheric chemistry: Volume I - gas phase reactions of O-x, HO_x, NO_x and SO_x species, *Atmos.*
564 *Chem. Phys.*, 4, 1461-1738, 2004.
- 565 Atlas, E.: EVIDENCE FOR GREATER-THAN-OR-EQUAL-TO-C-3 ALKYL NITRATES IN RURAL AND REMOTE
566 ATMOSPHERES, *Nature*, 331, 426-428, 1988.
- 567 Atlas, E., Pollock, W., Greenberg, J., Heidt, L., and Thompson, A. M.: ALKYL NITRATES, NONMETHANE HYDROCARBONS,
568 AND HALOCARBON GASES OVER THE EQUATORIAL PACIFIC-OCEAN DURING SAGA-3, *J. Geophys. Res.-Atmos.*, 98,
569 16933-16947, 1993.
- 570 Berkemeier, T., Ammann, M., Mentel, T. F., Poschl, U., and Shiraiwa, M.: Organic Nitrate Contribution to New Particle Formation and
571 Growth in Secondary Organic Aerosols from alpha-Pinene Ozonolysis, *Environ. Sci. Technol.*, 50, 6334-6342, 2016.
- 572 Blanchard, P., Shepson, P. B., Schiff, H. I., and Drummond, J. W.: DEVELOPMENT OF A GAS-CHROMATOGRAPH FOR TRACE-
573 LEVEL MEASUREMENT OF PEROXYACETYL NITRATE USING CHEMICAL AMPLIFICATION, *Anal. Chem.*, 65, 2472-2477,
574 1993.
- 575 Chen, J. and Venables, D. S.: A broadband optical cavity spectrometer for measuring weak near-ultraviolet absorption spectra of gases,
576 *Atmos. Meas. Tech.*, 4, 425-436, 2011.
- 577 Chen, J., Wu, H., Liu, A. W., Hu, S. M., and Zhang, J.: Field Measurement of NO₂ and RNO₂ by Two-Channel Thermal Dissociation
578 Cavity Ring Down Spectrometer, *Chinese J Chem Phys*, 30, 493-498, 2017.
- 579 Chuck, A. L., Turner, S. M., and Liss, P. S.: Direct evidence for a marine source of C-1 and C-2 alkyl nitrates, *Science*, 297, 1151-1154,
580 2002.
- 581 Day, D. A., Wooldridge, P. J., Dillon, M. B., Thornton, J. A., and Cohen, R. C.: A thermal dissociation laser-induced fluorescence
582 instrument for in situ detection of NO₂, peroxy nitrates, alkyl nitrates, and HNO₃, *J. Geophys. Res.-Atmos.*, 107, 2002.
- 583 Duan, J., Qin, M., Ouyang, B., Fang, W., Li, X., Lu, K. D., Tang, K., Liang, S. X., Meng, F. H., Hu, Z. K., Xie, P. H., Liu, W. Q., and
584 Hasler, R.: Development of an incoherent broadband cavity-enhanced absorption spectrometer for in situ measurements of HONO and
585 NO₂, *Atmos. Meas. Tech.*, 11, 4531-4543, 2018.
- 586 Fiedler, S. E., Hese, A., and Ruth, A. A.: Incoherent broad-band cavity-enhanced absorption spectroscopy, *Chem Phys Lett*, 371, 284-
587 294, 2003.
- 588 Fischer, R. G., Kastler, J., and Ballschmiter, K.: Levels and pattern of alkyl nitrates, multifunctional alkyl nitrates, and halocarbons in
589 the air over the Atlantic Ocean, *J. Geophys. Res.-Atmos.*, 105, 14473-14494, 2000.
- 590 Flocke, F. M., Weinheimer, A. J., Swanson, A. L., Roberts, J. M., Schmitt, R., and Shertz, S.: On the measurement of PANs by gas
591 chromatography and electron capture detection, *J. Atmos. Chem.*, 52, 19-43, 2005.
- 592 Friedrich, N., Tadic, I., Schuladen, J., Brooks, J., Darbyshire, E., Drewnick, F., Fischer, H., Lelieveld, J., and Crowley, J. N.:
593 Measurement of NO_x and NO_y with a thermal dissociation cavity ring-down spectrometer (TD-CRDS): instrument characterisation and
594 first deployment, *Atmos. Meas. Tech.*, 13, 5739-5761, 2020.
- 595 Fuchs, H., Holland, F., and Hofzumahaus, A.: Measurement of tropospheric RO₂ and HO₂ radicals by a laser-induced fluorescence
596 instrument, *Rev. Sci. Instrum.*, 79, 12, 2008.
- 597 Gaffney, J. S., Bornick, R. M., Chen, Y. H., and Marley, N. A.: Capillary gas chromatographic analysis of nitrogen dioxide and PANs
598 with luminol chemiluminescent detection, *Atmos. Environ.*, 32, 1445-1454, 1998.
- 599 Gherman, T., Venables, D. S., Vaughan, S., Orphal, J., and Ruth, A. A.: Incoherent broadband cavity-enhanced absorption spectroscopy
600 in the near-ultraviolet: Application to HONO and NO₂, *Environ. Sci. Technol.*, 42, 890-895, 2008.
- 601 Glavas, S. and Moschonas, N.: Determination of PAN, PPN, PnBN and selected pentyl nitrates in Athens, Greece, *Atmos. Environ.*, 35,
602 5467-5475, 2001.



- 603 Hao, C. S., Shepson, P. B., Drummond, J. W., and Muthuramu, K.: GAS-CHROMATOGRAPHIC DETECTOR FOR SELECTIVE AND
604 SENSITIVE DETECTION OF ATMOSPHERIC ORGANIC NITRATES, *Anal. Chem.*, 66, 3737-3743, 1994.
- 605 Horowitz, L. W., Fiore, A. M., Milly, G. P., Cohen, R. C., Perring, A., Wooldridge, P. J., Hess, P. G., Emmons, L. K., and Lamarque, J.
606 F.: Observational constraints on the chemistry of isoprene nitrates over the eastern United States, *J. Geophys. Res.-Atmos.*, 112, 13,
607 2007.
- 608 Jordan, N. and Osthoff, H. D.: Quantification of nitrous acid (HONO) and nitrogen dioxide (NO₂) in ambient air by broadband cavity-
609 enhanced absorption spectroscopy (IBBCEAS) between 361 and 388 nm, *Atmos. Meas. Tech.*, 13, 273-285, 2020.
- 610 Jordan, N., Ye, C. Z., Ghosh, S., Washenfelder, R. A., Brown, S. S., and Osthoff, H. D.: A broadband cavity-enhanced spectrometer for
611 atmospheric trace gas measurements and Rayleigh scattering cross sections in the cyan region (470-540 nm), *Atmos. Meas. Tech.*, 12,
612 1277-1293, 2019.
- 613 Kastler, J. and Ballschmiter, K.: Identification of alkyl dinitrates in ambient air of Central Europe, *Fresenius J. Anal. Chem.*, 363, 1-4,
614 1999.
- 615 Kirchner, F., Mayer-Figge, A., Zabel, F., and Becker, K. H.: Thermal stability of peroxy nitrates, *Int. J. Chem. Kinet.*, 31, 127-144, 1999.
- 616 Langridge, J. M., Ball, S. M., and Jones, R. L.: A compact broadband cavity enhanced absorption spectrometer for detection of
617 atmospheric NO₂ using light emitting diodes, *Analyst*, 131, 916-922, 2006.
- 618 Langridge, J. M., Ball, S. M., Shillings, A. J. L., and Jones, R. L.: A broadband absorption spectrometer using light emitting diodes for
619 ultrasensitive, in situ trace gas detection, *Rev. Sci. Instrum.*, 79, 2008.
- 620 Lee, B. H., Mohr, C., Lopez-Hilfiker, F. D., Lutz, A., Hallquist, M., Lee, L., Romer, P., Cohen, R. C., Iyer, S., Kurten, T., Hu, W., Day,
621 D. A., Campuzano-Jost, P., Jimenez, J. L., Xu, L., Ng, N. L., Guo, H., Weber, R. J., Wild, R. J., Brown, S. S., Koss, A., de Gouw, J.,
622 Olson, K., Goldstein, A. H., Seco, R., Kim, S., McAvey, K., Shepson, P. B., Starn, T., Baumann, K., Edgerton, E. S., Liu, J., Shilling, J.
623 E., Miller, D. O., Brune, W., Schobesberger, S., D'Ambro, E. L., and Thornton, J. A.: Highly functionalized organic nitrates in the
624 southeast United States: Contribution to secondary organic aerosol and reactive nitrogen budgets, *Proc. Natl. Acad. Sci. U. S. A.*, 113,
625 1516-1521, 2016.
- 626 Lee, L., Wooldridge, P. J., Gilman, J. B., Warneke, C., de Gouw, J., and Cohen, R. C.: Low temperatures enhance organic nitrate formation:
627 evidence from observations in the 2012 Uintah Basin Winter Ozone Study, *Atmos. Chem. Phys.*, 14, 12441-12454, 2014.
- 628 Li, Z., Hu, R., Xie, P., Chen, H., Wu, S., Wang, F., Wang, Y., Ling, L., Liu, J., and Liu, W.: Development of a portable cavity ring down
629 spectroscopy instrument for simultaneous, in situ measurement of NO₃ and N₂O₅, *Opt. Express*, 26, A433-A449, 2018.
- 630 Liang, S., Qin, M., Xie, P., Duan, J., Fang, W., He, Y., Xu, J., Liu, J., Li, X., Tang, K., Meng, F., Ye, K., Liu, J., and Liu, W.: Development
631 of an incoherent broadband cavity-enhanced absorption spectrometer for measurements of ambient glyoxal and NO₂ in a polluted urban
632 environment, *Atmos. Meas. Tech.*, 12, 2499-2512, 2019.
- 633 Liu, J., Li, X., Yang, Y., Wang, H., Wu, Y., Lu, X., Chen, M., Hu, J., Fan, X., Zeng, L., and Zhang, Y.: An IBBCEAS system for
634 atmospheric measurements of glyoxal and methylglyoxal in the presence of high NO₂ concentrations, *Atmos. Meas. Tech.*, 12, 4439-
635 4453, 2019.
- 636 Luxenhofer, O., Schneider, E., and Ballschmiter, K.: SEPARATION, DETECTION AND OCCURRENCE OF (C₂-C₈)-ALKYL
637 NITRATES AND PHENYL-ALKYL NITRATES AS TRACE COMPOUNDS IN CLEAN AND POLLUTED AIR, *Fresenius J. Anal.
638 Chem.*, 350, 384-394, 1994.
- 639 Ma, M., Gao, Y., Wang, Y., Zhang, S., Leung, L. R., Liu, C., Wang, S., Zhao, B., Chang, X., Su, H., Zhang, T., Sheng, L., Yao, X., and
640 Gao, H.: Substantial ozone enhancement over the North China Plain from increased biogenic emissions due to heat waves and land cover
641 in summer 2017, *Atmos. Chem. Phys.*, 19, 12195-12207, 2019.
- 642 Mellouki, A., Wallington, T. J., and Chen, J.: Atmospheric Chemistry of Oxygenated Volatile Organic Compounds: Impacts on Air
643 Quality and Climate, *Chemical Reviews*, 115, 3984-4014, 2015.
- 644 Min, K. E., Washenfelder, R. A., Dube, W. P., Langford, A. O., Edwards, P. M., Zarzana, K. J., Stutz, J., Lu, K., Rohrer, F., Zhang, Y.,
645 and Brown, S. S.: A broadband cavity enhanced absorption spectrometer for aircraft measurements of glyoxal, methylglyoxal, nitrous
646 acid, nitrogen dioxide, and water vapor, *Atmos Meas Tech*, 9, 423-440, 2016.



- 647 Ng, N. L., Brown, S. S., Archibald, A. T., Atlas, E., Cohen, R. C., Crowley, J. N., Day, D. A., Donahue, N. M., Fry, J. L., Fuchs, H.,
648 Griffin, R. J., Guzman, M. I., Herrmann, H., Hodzic, A., Iinuma, Y., Jimenez, J. L., Kiendler-Scharr, A., Lee, B. H., Luecken, D. J., Mao,
649 J. Q., McLaren, R., Mutzel, A., Osthoff, H. D., Ouyang, B., Picquet-Varrault, B., Platt, U., Pye, H. O. T., Rudich, Y., Schwantes, R. H.,
650 Shiraiwa, M., Stutz, J., Thornton, J. A., Tilgner, A., Williams, B. J., and Zaveri, R. A.: Nitrate radicals and biogenic volatile organic
651 compounds: oxidation, mechanisms, and organic aerosol, *Atmos Chem Phys*, 17, 2103-2162, 2017.
- 652 Paul, D., Furgeson, A., and Osthoff, H. D.: Measurements of total peroxy and alkyl nitrate abundances in laboratory-generated gas
653 samples by thermal dissociation cavity ring-down spectroscopy, *Rev. Sci. Instrum.*, 80, 2009.
- 654 Paul, D. and Osthoff, H. D.: Absolute Measurements of Total Peroxy Nitrate Mixing Ratios by Thermal Dissociation Blue Diode Laser
655 Cavity Ring-Down Spectroscopy, *Anal Chem*, 82, 6695-6703, 2010.
- 656 Perring, A. E., Bertram, T. H., Wooldridge, P. J., Fried, A., Heikes, B. G., Dibb, J., Crouse, J. D., Wennberg, P. O., Blake, N. J., Blake,
657 D. R., Brune, W. H., Singh, H. B., and Cohen, R. C.: Airborne observations of total RONO₂: new constraints on the yield and lifetime
658 of isoprene nitrates, *Atmos. Chem. Phys.*, 9, 1451-1463, 2009.
- 659 Perring, A. E., Pusede, S. E., and Cohen, R. C.: An Observational Perspective on the Atmospheric Impacts of Alkyl and Multifunctional
660 Nitrates on Ozone and Secondary Organic Aerosol, *Chemical Reviews*, 113, 5848-5870, 2013.
- 661 Reisen, F., Aschmann, S. M., Atkinson, R., and Arey, J.: 1,4-hydroxycarbonyl products of the OH radical initiated reactions of C-5-C-8
662 n-alkanes in the presence of NO, *Environ. Sci. Technol.*, 39, 4447-4453, 2005.
- 663 Roberts, J. M.: THE ATMOSPHERIC CHEMISTRY OF ORGANIC NITRATES, *Atmospheric Environment Part a-General Topics*, 24,
664 243-287, 1990.
- 665 Roberts, J. M., Bertman, S. B., Parrish, D. D., Fehsenfeld, F. C., Jobson, B. T., and Niki, H.: Measurement of alkyl nitrates at Chebogue
666 Point, Nova Scotia during the 1993 North Atlantic Regional Experiment (NARE) intensive, *J. Geophys. Res.-Atmos.*, 103, 13569-13580,
667 1998a.
- 668 Roberts, J. M., Jobson, B. T., Kuster, W., Goldan, P., Murphy, P., Williams, E., Frost, G., Riemer, D., Apel, E., Stroud, C., Wiedinmyer,
669 C., and Fehsenfeld, F.: An examination of the chemistry of peroxy-carboxylic nitric anhydrides and related volatile organic compounds
670 during Texas Air Quality Study 2000 using ground-based measurements, *J. Geophys. Res.-Atmos.*, 108, 2003.
- 671 Roberts, J. M., Williams, J., Baumann, K., Buhr, M. P., Goldan, P. D., Holloway, J., Hubler, G., Kuster, W. C., McKeen, S. A., Ryerson,
672 T. B., Trainer, M., Williams, E. J., Fehsenfeld, F. C., Bertman, S. B., Nouaime, G., Seaver, C., Grodzinsky, G., Rodgers, M., and Young,
673 V. L.: Measurements of PAN, PPN, and MPAN made during the 1994 and 1995 Nashville Intensives of the Southern Oxidant Study:
674 Implications for regional ozone production from biogenic hydrocarbons, *J. Geophys. Res.-Atmos.*, 103, 22473-22490, 1998b.
- 675 Rollins, A. W., Browne, E. C., Min, K. E., Pusede, S. E., Wooldridge, P. J., Gentner, D. R., Goldstein, A. H., Liu, S., Day, D. A., Russell,
676 L. M., and Cohen, R. C.: Evidence for NO_x Control over Nighttime SOA Formation, *Science*, 337, 1210-1212, 2012.
- 677 Russell, M. and Allen, D. T.: Predicting secondary organic aerosol formation rates in southeast Texas, *J Geophys Res-Atmos*, 110, 2005.
- 678 Sadanaga, Y., Takaji, R., Ishiyama, A., Nakajima, K., Matsuki, A., and Bandow, H.: Thermal dissociation cavity attenuated phase shift
679 spectroscopy for continuous measurement of total peroxy and organic nitrates in the clean atmosphere, *Rev. Sci. Instrum.*, 87, 2016.
- 680 Shardanand, S. a. R., A. D. P.: Absolute Rayleigh scattering cross sections of gases and freons of stratospheric interest in the visible and
681 ultraviolet regions, *NASA Technical Note*, 1977. 1977.
- 682 Shu, L., Wang, T., Han, H., Xie, M., Chen, P., Li, M., and Wu, H.: Summertime ozone pollution in the Yangtze River Delta of eastern
683 China during 2013-2017: Synoptic impacts and source apportionment, *Environmental pollution (Barking, Essex : 1987)*, doi:
684 10.1016/j.envpol.2019.113631, 2019. 113631-113631, 2019.
- 685 Simpson, I. J., Wang, T., Guo, H., Kwok, Y. H., Flocke, F., Atlas, E., Meinardi, S., Rowland, F. S., and Blake, D. R.: Long-term
686 atmospheric measurements of C-1-C-5 alkyl nitrates in the pearl river delta region of southeast China, *Atmos Environ*, 40, 1619-1632,
687 2006.
- 688 Slusher, D. L., Huey, L. G., Tanner, D. J., Flocke, F. M., and Roberts, J. M.: A thermal dissociation-chemical ionization mass spectrometry
689 (TD-CIMS) technique for the simultaneous measurement of peroxyacyl nitrates and dinitrogen pentoxide, *J Geophys Res-Atmos*, 109,
690 2004.



- 691 Sneep, M. and Ubachs, W.: Direct measurement of the Rayleigh scattering cross section in various gases, *J. Quant. Spectrosc. Radiat.*
692 *Transf.*, 92, 293-310, 2005.
- 693 Sobanski, N., Schuladen, J., Schuster, G., Lelieveld, J., and Crowley, J. N.: A five-channel cavity ring-down spectrometer for the
694 detection of NO₂, NO₃, N₂O₅, total peroxy nitrates and total alkyl nitrates, *Atmos. Meas. Tech.*, 9, 5103-5118, 2016.
- 695 Sobanski, N., Thieser, J., Schuladen, J., Sauvage, C., Song, W., Williams, J., Lelieveld, J., and Crowley, J. N.: Day and night- time
696 formation of organic nitrates at a forested mountain site in south-west Germany, *Atmos Chem Phys*, 17, 4115-4130, 2017.
- 697 Song, J., Zhang, Y., Huang, Y., Ho, K. F., Yuan, Z., Ling, Z., Niu, X., Gao, Y., Cui, L., Louie, P. K. K., Lee, S.-c., and Lai, S.: Seasonal
698 variations of C-1-C-4 alkyl nitrates at a coastal site in Hong Kong: Influence of photochemical formation and oceanic emissions,
699 *Chemosphere*, 194, 275-284, 2018.
- 700 Sun, J., Li, Z., Xue, L., Wang, T., Wang, X., Gao, J., Nie, W., Simpson, I. J., Gao, R., Blake, D. R., Chai, F., and Wang, W.: Summertime
701 C-1-C-5 alkyl nitrates over Beijing, northern China: Spatial distribution, regional transport, and formation mechanisms, *Atmos. Res.*,
702 204, 102-109, 2018.
- 703 Talbot, R. W., Dibb, J. E., Scheuer, E. M., Bradshaw, J. D., Sandholm, S. T., Singh, H. B., Blake, D. R., Blake, N. J., Atlas, E., and
704 Flocke, F.: Tropospheric reactive odd nitrogen over the South Pacific in austral springtime, *J. Geophys. Res.-Atmos.*, 105, 6681-6694,
705 2000.
- 706 Tang, K., Qin, M., Fang, W., Duan, J., Meng, F., Ye, K., Zhang, H., Xie, P., He, Y., Xu, W., Liu, J., and Liu, W.: Simultaneous detection
707 of atmospheric HONO and NO₂ utilising an IBBCEAS system based on an iterative algorithm, *Atmos. Meas. Tech.*, 13, 6487-6499,
708 2020.
- 709 Tanimoto, H., Hirokawa, J., Kajii, Y., and Akimoto, H.: A new measurement technique of peroxyacetyl nitrate at parts per trillion by
710 volume levels: Gas chromatography/negative ion chemical ionization mass spectrometry, *J. Geophys. Res.-Atmos.*, 104, 21343-21354,
711 1999.
- 712 Thalman, R., Baeza-Romero, M. T., Ball, S. M., Borrás, E., Daniels, M. J. S., Goodall, I. C. A., Henry, S. B., Karl, T., Keutsch, F. N.,
713 Kim, S., Mak, J., Monks, P. S., Muñoz, A., Orlando, J., Peppe, S., Rickard, A. R., Rodenas, M., Sanchez, P., Seco, R., Su, L., Tyndall,
714 G., Vazquez, M., Vera, T., Waxman, E., and Volkamer, R.: Instrument intercomparison of glyoxal, methyl glyoxal and NO₂ under
715 simulated atmospheric conditions, *Atmos. Meas. Tech.*, 8, 1835-1862, 2015.
- 716 Thalman, R. and Volkamer, R.: Inherent calibration of a blue LED-CE-DOAS instrument to measure iodine oxide, glyoxal, methyl
717 glyoxal, nitrogen dioxide, water vapour and aerosol extinction in open cavity mode, *Atmos. Meas. Tech.*, 3, 1797-1814, 2010.
- 718 Thieser, J., Schuster, G., Schuladen, J., Phillips, G. J., Reiffs, A., Parchatka, U., Pöhler, D., Lelieveld, J., and Crowley, J. N.: A two-
719 channel thermal dissociation cavity ring-down spectrometer for the detection of ambient NO₂, RO₂NO₂ and RONO₂, *Atmos Meas Tech*,
720 9, 553-576, 2016.
- 721 Vandaele, A. C., Hermans, C., Fally, S., Carleer, M., Colin, R., Merienne, M. F., Jenouvrier, A., and Coquart, B.: High-resolution Fourier
722 transform measurement of the NO₂ visible and near-infrared absorption cross sections: Temperature and pressure effects, *J. Geophys.*
723 *Res.-Atmos.*, 107, 13, 2002.
- 724 Ventrillard-Courtillet, I., O'Brien, E. S., Kassi, S., Mejean, G., and Romanini, D.: Incoherent broad-band cavity-enhanced absorption
725 spectroscopy for simultaneous trace measurements of NO₂ and NO₃ with a LED source, *Appl. Phys. B-Lasers Opt.*, 101, 661-669, 2010.
- 726 Voigt, S., Orphal, J., and Burrows, J. P.: The temperature and pressure dependence of the absorption cross-sections of NO₂ in the 250-
727 800 nm region measured by Fourier-transform spectroscopy, *J Photoch Photobio A*, 149, 1-7, 2002.
- 728 Wang, H., Chen, J., and Lu, K.: Development of a portable cavity-enhanced absorption spectrometer for the measurement of ambient
729 NO₃ and N₂O₅: experimental setup, lab characterizations, and field applications in a polluted urban environment, *Atmos. Meas. Tech.*,
730 10, 1465-1479, 2017a.
- 731 Wang, T., Poon, C. N., Kwok, Y. H., and Li, Y. S.: Characterizing the temporal variability and emission patterns of pollution plumes in
732 the Pearl River Delta of China, *Atmos. Environ.*, 37, 3539-3550, 2003.
- 733 Wang, T., Wei, X. L., Ding, A. J., Poon, C. N., Lam, K. S., Li, Y. S., Chan, L. Y., and Anson, M.: Increasing surface ozone concentrations
734 in the background atmosphere of Southern China, 1994-2007, *Atmos Chem Phys*, 9, 6217-6227, 2009.



- 735 Wang, T., Xue, L., Brimblecombe, P., Lam, Y. F., Li, L., and Zhang, L.: Ozone pollution in China: A review of concentrations,
736 meteorological influences, chemical precursors, and effects, *Sci. Total Environ.*, 575, 1582-1596, 2017b.
- 737 Washenfelder, R. A., Langford, A. O., Fuchs, H., and Brown, S. S.: Measurement of glyoxal using an incoherent broadband cavity
738 enhanced absorption spectrometer, *Atmos. Chem. Phys.*, 8, 7779-7793, 2008.
- 739 Wennberg, P. O., Bates, K. H., Crounse, J. D., Dodson, L. G., McVay, R. C., Mertens, L. A., Nguyen, T. B., Praske, E., Schwantes, R.
740 H., Smarte, M. D., St Clair, J. M., Teng, A. P., Zhang, X., and Seinfeld, J. H.: Gas-Phase Reactions of Isoprene and Its Major Oxidation
741 Products, *Chemical Reviews*, 118, 3337-3390, 2018.
- 742 Wild, R. J., Edwards, P. M., Dube, W. P., Baumann, K., Edgerton, E. S., Quinn, P. K., Roberts, J. M., Rollins, A. W., Veres, P. R., Warneke,
743 C., Williams, E. J., Yuan, B., and Brown, S. S.: A Measurement of Total Reactive Nitrogen, NO_y, together with NO₂, NO, and O₃ via
744 Cavity Ring-down Spectroscopy, *Environ. Sci. Technol.*, 48, 9609-9615, 2014.
- 745 Womack, C. C., Neuman, J. A., Veres, P. R., Eilerman, S. J., Brock, C. A., Decker, Z. C. J., Zarzana, K. J., Dube, W. P., Wild, R. J.,
746 Wooldridge, P. J., Cohen, R. C., and Brown, S. S.: Evaluation of the accuracy of thermal dissociation CRDS and LIF techniques for
747 atmospheric measurement of reactive nitrogen species, *Atmos Meas Tech*, 10, 1911-1926, 2017.
- 748 Wooldridge, P. J., Perring, A. E., Bertram, T. H., Flocke, F. M., Roberts, J. M., Singh, H. B., Huey, L. G., Thornton, J. A., Wolfe, G. M.,
749 Murphy, J. G., Fry, J. L., Rollins, A. W., LaFranchi, B. W., and Cohen, R. C.: Total Peroxy Nitrates (Sigma PNs) in the atmosphere: the
750 Thermal Dissociation-Laser Induced Fluorescence (TD-LIF) technique and comparisons to speciated PAN measurements, *Atmos. Meas.*
751 *Tech.*, 3, 593-607, 2010.
- 752 Yang, Y., Li, X., Zu, K., Lian, C., Chen, S., Dong, H., Feng, M., Liu, H., Liu, J., Lu, K., Lu, S., Ma, X., Song, D., Wang, W., Yang, S.,
753 Yang, X., Yu, X., Zhu, Y., Zeng, L., Tan, Q., and Zhang, Y.: Elucidating the effect of HONO on O₃ pollution by a case study in southwest
754 China, *The Science of the total environment*, doi: 10.1016/j.scitotenv.2020.144127, 2020. 144127-144127, 2020.
- 755 Yi, H. M., Wu, T., Wang, G. S., Zhao, W. X., Fertein, E., Coeur, C., Gao, X. M., Zhang, W. J., and Chen, W. D.: Sensing atmospheric
756 reactive species using light emitting diode by incoherent broadband cavity enhanced absorption spectroscopy, *Opt. Express*, 24, 10, 2016.
- 757 Yin, C., Deng, X., Zou, Y., Solmon, F., Li, F., and Deng, T.: Trend analysis of surface ozone at suburban Guangzhou, China, *Sci. Total*
758 *Environ.*, 695, 2019.
- 759 Zare, A., Romer, P. S., Tran, N., Keutsch, F. N., Skog, K., and Cohen, R. C.: A comprehensive organic nitrate chemistry: insights into
760 the lifetime of atmospheric organic nitrates, *Atmos. Chem. Phys.*, 18, 15419-15436, 2018.
- 761 Zhang, Y., Sun, J., Zheng, P., Chen, T., Liu, Y., Han, G., Simpson, I. J., Wang, X., Blake, D. R., Li, Z., Yang, X., Qi, Y., Wang, Q., Wang,
762 W., and Xue, L.: Observations of C₁-C₅ alkyl nitrates in the Yellow River Delta, northern China: Effects of biomass burning and oil
763 field emissions, *The Science of the total environment*, 656, 129-139, 2018.
- 764